

Research Paper

Cite this article: Deng M (2020). High-efficiency antenna-to-antenna polarization converters for customized polarization angle deflection. *International Journal of Microwave and Wireless Technologies* **12**, 688–694. <https://doi.org/10.1017/S175907872000001X>

Received: 31 August 2019
Revised: 22 December 2019
Accepted: 8 January 2020
First published online: 10 February 2020


Key words:

Split ring resonators; polarization conversion; antenna-to-antenna; customized angle deflection

Author for correspondence:

Manlan Deng,
E-mail: deng-manlan@163.com

High-efficiency antenna-to-antenna polarization converters for customized polarization angle deflection

Manlan Deng 

College of Physical Science and Technology of Yichun University, Yichun 336000, Jiangxi, China

Abstract

In this paper, an antenna-to-antenna method to design high-efficiency polarization converters was proposed. Two in-linked split ring resonators (SRRs) were used as the fundamental unit cell, which can effectively make the original linear polarization angle deflected into a customized one (include but not limited to 90°). The same as the process of energy reception and transmitting of microstrip symmetric dipole antennas, the top SRR plays the role of a receiving antenna and the bottom one acts as a transmitting antenna. Under normal illumination, the strong coupling between electric resonance and magnetic resonance can result in high transmission and broad bandwidth. Since the two SRRs act as two independently polarization selective components, the polarization angle of transmitted waves can be easily controlled by rotating the transmitting SRRs around the center. The proposed concept and the design method are validated using numerical simulations, as well as experimental results of three examples for 45, 60 and 90° polarization angle rotation, the polarization conversion ratio of which is about 92.2, 88.9 and 91.9% from 7.5 to 10 GHz.

Introduction

Polarization of electromagnetic waves [1] is one of the most important properties in practical wireless communications, which has greatly affected our daily life, from consumer products to high-tech applications. As is known to all, good polarization matching greatly contributes to improve the efficiency of energy reception and reduce unexpected loss. However, this is always hardly realized since the varied spatial position of antenna platforms. Thus, it is necessary to find a method to modulate or convert the polarization state. Moreover, phase changes caused in the process of polarization conversion also possess a lot of application value, such as surface wave coupler [2], anomalous reflection, refraction [3–5], etc.

In the microwave regime, to deflect the polarization angle, mirrored broken-symmetric structures have been widely adopted to design linear-to-linear polarization converters (LLPCs) [6, 7] since they can generate phase difference in two in-plane directions. As an example, the authors in [8] inserted a cut-wire array into two orthogonal metallic gratings and finally designed a transmissive converter for cross-polarization conversion. Due to multiple constructive interferences caused by Fabry–Perot-like resonance [9, 10], their configuration exhibits more than 80% linear polarization conversion efficiency in an ultra-wide bandwidth. This concept is then expanded to reflective polarization conversion formed by varied metallic cur-wire patterns [11–14]. As an example, a number of metallic double-headed arrows were applied to design a reflective metasurface for linear cross-polarization conversion [15]. Constructive interferences and multiple plasmon resonances finally resulted in ultra-wideband operating bandwidth and high polarization conversion efficiency. With the deepening of research, polarization conversion metasurfaces with different phase distributions have been gradually applied in areas of beam steering and shaping [16], asymmetric transmission [17, 18], radar cross-section reduction [19, 20], etc. Moreover, chiral structures have also been demonstrated to be capable of converting linear polarization into circular polarization [21–24]. However, as mentioned above, most published LLPCs focused on how to high-efficiently realize cross-polarization conversion, namely, converting the original polarization state into its orthogonal one. This is obviously insufficient for the diverse needs in practical applications. Thus, it is necessary to find a way to high-efficiently convert the original linear polarization angle into another customized one.

To this end, a high-efficiency LLPC for customized polarization angle rotation is proposed and verified. The converter is composed of periodic subwavelength split ring resonators (SRRs), which are in-linked by coaxial lines. Each pair of top and bottom SRRs acts as a pair of microstrip symmetric dipole antennas for energy reception and transmission. As a result, customized polarization angle can be easily obtained by rotating the bottom transmitting SRR with a corresponding angle. Moreover, since the strong coupling between the electric

and magnetic resonances, the proposed converter has also been proven to be characterized with a very high polarization conversion ratio (PCR).

The principle for customized polarization angle deflection

For explaining linear polarization conversion transmission, let us consider an incoming y -polarized plane wave normally propagating from $+z$ to the $-z$ direction, the electric field of reflected wave is simply expressed as

$$E^r(r, t) = (R_{yy} + R_{xy})e^{i(-kz - \omega t)} \tag{1}$$

where ω , k , R_{yy} , and R_{xy} represent the frequency, wave vector and complex reflection coefficient, respectively. On the other hand, the transmitted wave can be divided into two parts (T_{yy} and T_{xy}) and the electric field passing through the polarization converter can be expressed as equation (2):

$$E^t(r, t) = (T_{yy} + T_{xy})e^{i(kz - \omega t)} \tag{2}$$

where T_{yy} and T_{xy} denote complex transmission coefficients of y -polarized and x -polarized transmitted waves. The amplitudes of the transmission coefficients are presented by t_{yy} and t_{xy} , respectively. The phases of the transmission coefficients are given by δ_x and δ_y . The transmitted electric field is thus to be further described in equation (3):

$$E^t(r, t) = (\vec{x}t_{xy}e^{j\delta_x} + \vec{y}t_{yy}e^{j\delta_y})e^{i(kz - \omega t)} \tag{3}$$

$$\Delta = \delta_x - \delta_y \tag{4}$$

The phase difference Δ between the x - and y -components of the transmitted electric fields is presented by equation (4). Three possible effects are resulted under normal y -polarized incidence. (i) When $\Delta = \pm\pi/2$ and $t_{yy} = t_{xy}$, the transmitted wave belongs to circular polarization, where “+” is for left-handed circular polarization and “-” for right-handed circular polarization. (ii) When $\Delta = \pm\pi/2$ but $t_{yy} \neq t_{xy}$, elliptical polarization transmitted wave can be obtained. (iii) When $\Delta = 0$ or π , the transmitted field is characterized with linear polarization state. The polarization angle Φ can be worked out by

$$\Phi = \arctan \frac{t_{xy}}{t_{yy}} \tag{5}$$

The amplitude of the converted transmission coefficient is then calculated by

$$t_{\Phi y} = \sqrt{t_{yy}^2 + t_{xy}^2} \tag{6}$$

Design and simulated analysis

The unit cell of the proposed transmissive polarization converter is shown in Fig. 1, which is a five-layered structure. For the first layer, a metallic SRR symmetric with respect to the y -axis is adopted as the receiving antenna. Both second and fourth layers are intermediate dielectric substrates. The middle layer is a continuous metallic sheet decorated with a circular hole. The bottom layer is an equal-sized transmitting SRR, which is linked with the

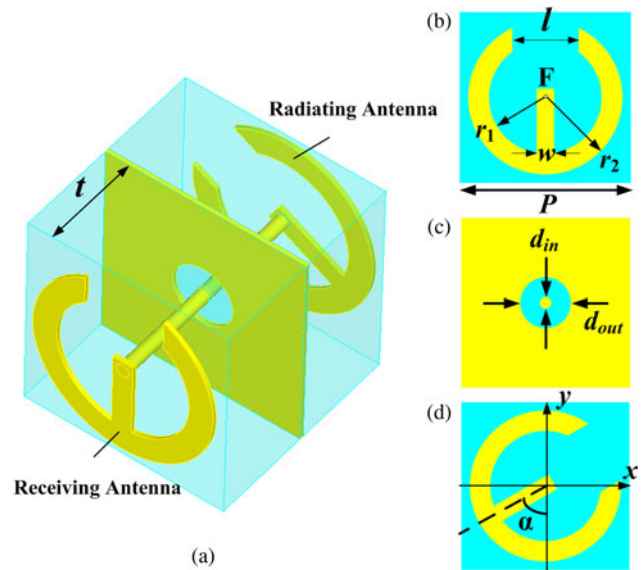


Fig. 1. (a) The schematic diagram of the unit cell and the front views and geometric parameters of (b) the top layer, (c) the middle layer, and (d) the bottom layer.

top one by a coaxial line through the center of the overall structure. The thickness of the dielectric substrates and the diameter of circular hole on the metal sheet mainly contribute to control the amplitude of transmission waves. On the other hand, the operating frequency bandwidth is controlled by adjusting or tailoring the dimensions of metallic SRRs. The deflected polarization angle is determined by the rotation angle of the transmitting SRR.

First, the unit cell with $\alpha = 60^\circ$ is computed using commercial microwave software CST to verify 60° polarization angle deflection. Both conditions along the x - and y -directions are set as “Unit Cell,” while “Open Add Space” is adopted along the z -direction. Considering y -polarized waves normally illuminate upon the top SRRs from $+z$ to the $-z$ axis. After systematical optimization, the geometric parameters are finally fixed as the inner radius $r_1 = 4.5$ mm, the outer radius $r_2 = 3.3$ mm, the width of split $l = 3.9$ mm, and the width of connected line $w = 1$ mm, respectively. The periodicity of each unit cell is set to be $P = 10$ mm. Each F4B dielectric layer is as thin as 2.0 mm, the dielectric constant and loss tangent of which are $\epsilon_r = 2.65$ and $\tan \delta = 0.001$. The diameters of circular hole and the metallic via are $d_{out} = 3$ mm and $d_{in} = 0.65$ mm.

Concluded from the results indicated in Fig. 2(a), the frequency interval for good impedance matching covers from 7.5 to 10 GHz, where the specular R_{yy} and R_{xy} in dB are lower than -10 and -30 dB, respectively. This means most energy has been transmitted through the unit cell, while only little energy has been converted into x -polarization and reflected back. Accordingly, two components T_{xy} and T_{yy} in dB are averagely -1.52 and -6.22 dB. The simulated phase distributions of T_{xy} and T_{yy} are plotted in the Fig. 2(b). Within the corresponding operation frequency band, the phase difference Δ is nearly equal to zero, which indicates the two components remain orthogonal. Thus, the $T_{\Phi y}$ in dB can be then calculated by adding two components T_{xy} and T_{yy} . From the violet curve plotted in Fig. 2(a), it is more than -0.5 dB from 7.5 to 10 GHz. To comprehensively evaluate the conversion efficiency and eliminate dielectric loss, according to [17], the PCR for the proposed converter can be expressed as $PCR = (t_{xy}^2 + t_{yy}^2) / (t_{xy}^2 + t_{yy}^2 + r_{xy}^2 + r_{yy}^2)$. The post processed PCR in the

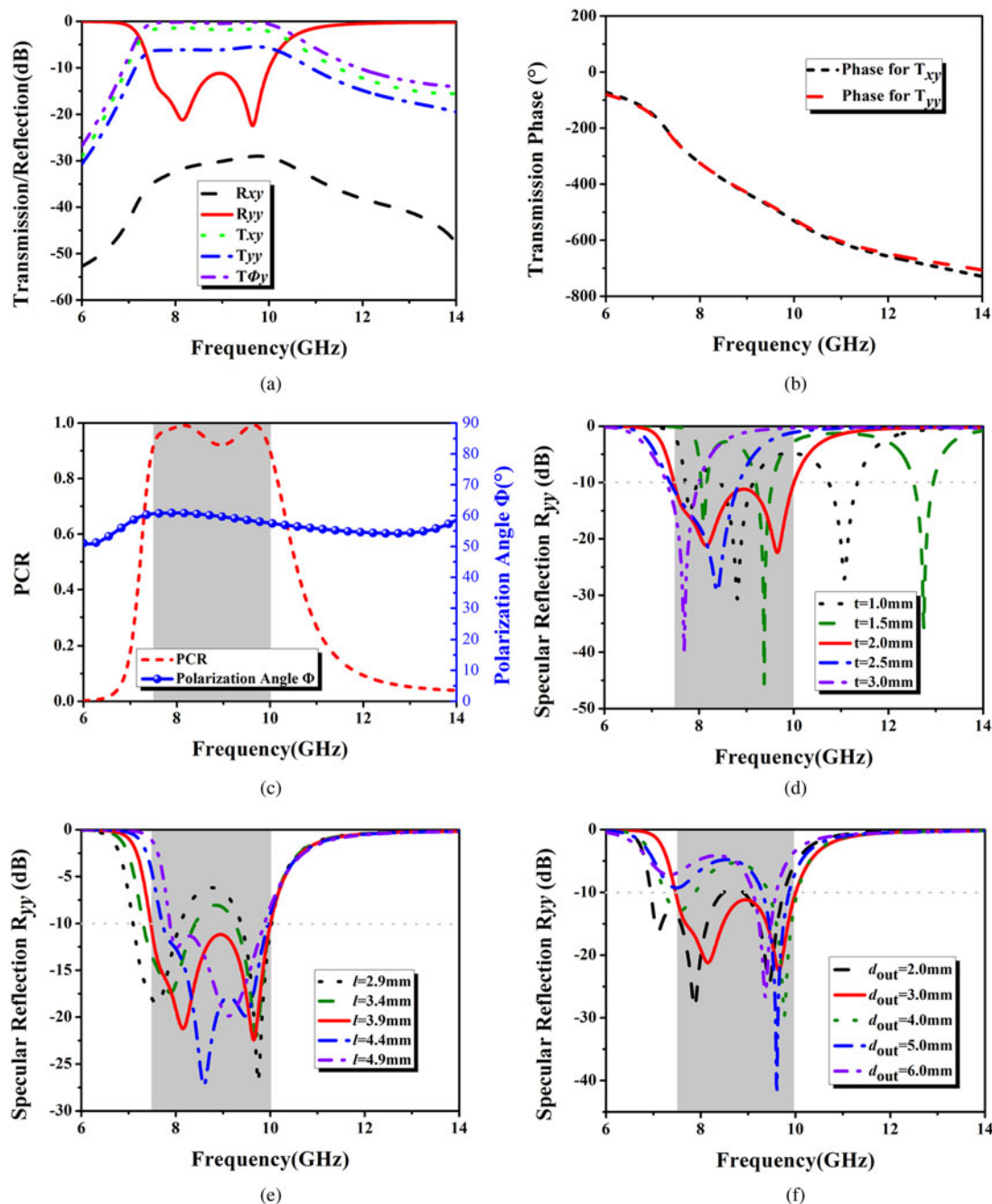


Fig. 2. (a) The specular reflection coefficients for R_{xy} , R_{yy} in dB and normal transmission coefficients for T_{xy} and T_{yy} in dB; (b) phase distributions for T_{xy} and T_{yy} ; (c) frequency response of the $T_{\phi y}$ and deflected polarization angle Φ ; (d), (e), and (f) specular reflection coefficients R_{yy} for different values of t , l , and d_{out} .

operating frequency band is more than 90%, as the red curve shown in Fig. 2(c). Additionally, the deflected polarization angle Φ can be further obtained by $\Phi = \arctan(t_{xy}/t_{yy})$. From the blue curve in Fig. 2(c), it could be seen the averaged Φ is about 59.8° , basically close to the rotation angle $\alpha = 60^\circ$. The slight errors are mainly caused by the amplitude fluctuations within the good impedance frequency range.

To investigate the influences of geometric parameters, the specular reflection coefficients R_{yy} for different values of t , l , and d_{out} are then simulated and comparatively analyzed. As indicated in Fig. 2(d)–2(f), the bandwidth of $R_{yy} < -10$ dB decrease with the increase of the dielectric thickness t from 1.0 to

3.0 mm. It is also clear to see less resonance dips with an increment in t . On the other hand, when the width of split w varies from 2.9 to 4.9 mm, the corresponding curves are gradually shift to the higher frequency regime. This mainly owes to the reductive electrical dimensions. Meanwhile, the effect of coupling between two adjacent resonances is strengthened and results in a continuous frequency band for good impedance matching. Besides, as the bridge between the receiving and transmitting SRRs, the value of the diameter d_{out} greatly influenced the efficiency of polarization conversion. For increasing values in d_{out} , the R_{yy} around the first resonance gradually increases more than -10 dB, whereas there is only little impact taking place at the second resonance.

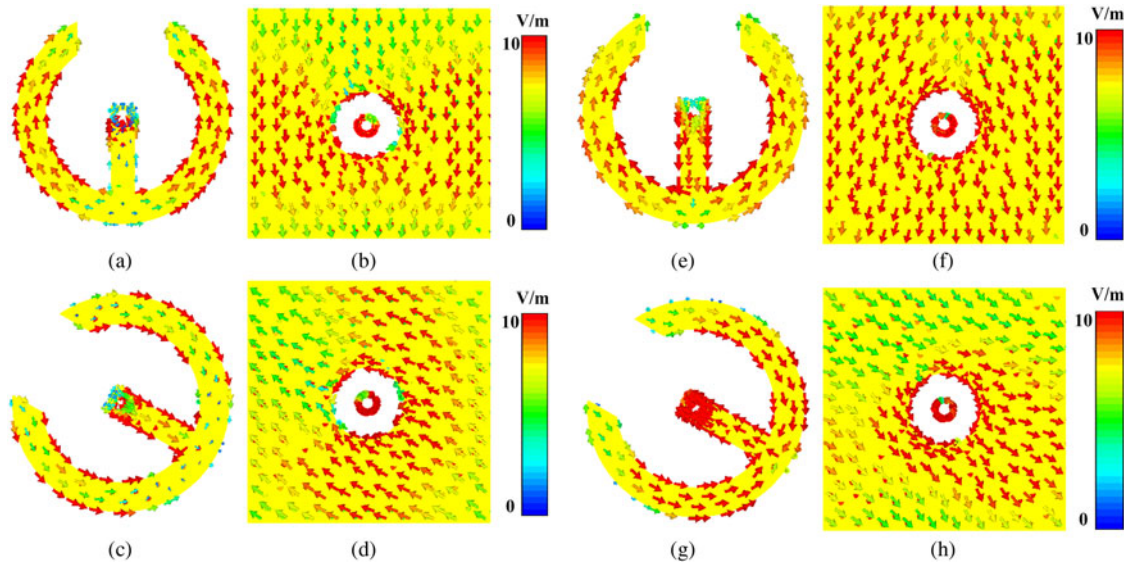


Fig. 3. The surface currents on the top and bottom SRRs: (a, b) and (c, d) for $f=8.2$ GHz and (e, f) and (g, h) for $f=9.6$ GHz.

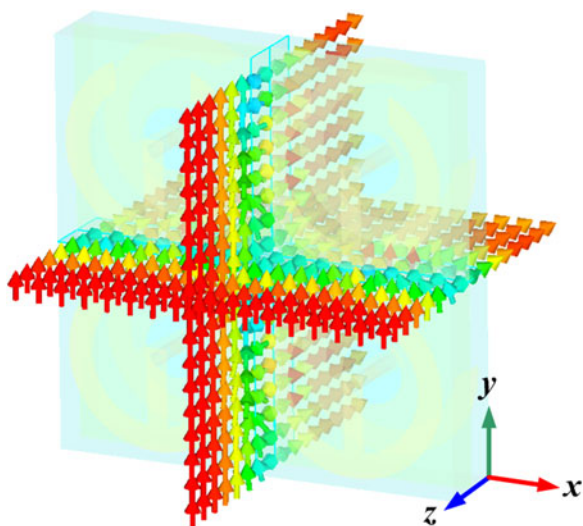


Fig. 4. The 3D E -field distributions at 9.6 GHz on the x - o - z plane and y - o - z plane.

It is well known that an electromagnetic field causes the excitation of an electric dipole with parallel currents and a magnetic dipole excited with anti-parallel currents. The interaction between a magnetic dipole and an electric dipole will result in strong coupling and high transmission. Thus, to further understand its broadband bandwidth, the surface currents at two resonance frequency points ($f=8.2$ and 9.6 GHz) are additionally monitored and illustrated in Fig. 3. It can be obviously seen that the currents on the metallic SRRs are symmetric with respect to the y -axis and the axis oriented to the rotation angle α , respectively. For the similar current distributions, the SRRs can be regarded as the microstrip symmetric dipole antennas. In detail, at $f=8.2$ GHz, the magnetic resonances are generated by anti-parallel surface currents induced along the rotated SRRs and the metallic plane, as shown in Fig. 3(c) and 3(d). However, at $f=9.6$ GHz, the electric resonance is generated by parallel surface currents, as indicated in Fig. 3(g) and 3(h). As for the receiving SRRs, surface currents remain anti-

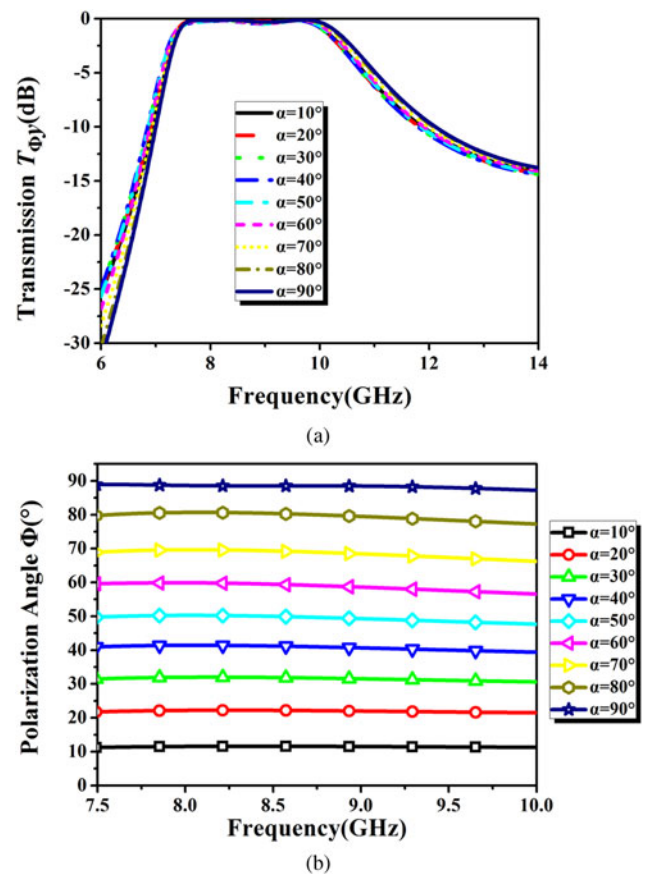


Fig. 5. (a) The normal transmission coefficient $T_{\Phi y}$ in dB and (b) the deflected polarization angle Φ distributions when the rotation angle α varies from 10 to 90° .

parallel at both resonance frequency points, as shown in Fig. 3(a), 3(b) and 3(e), 3(f). The wide-band and high-efficiency performance results from the superposition of two polarization conversion peaks around 8.2 and 9.6 GHz corresponding to the two resonant frequencies.

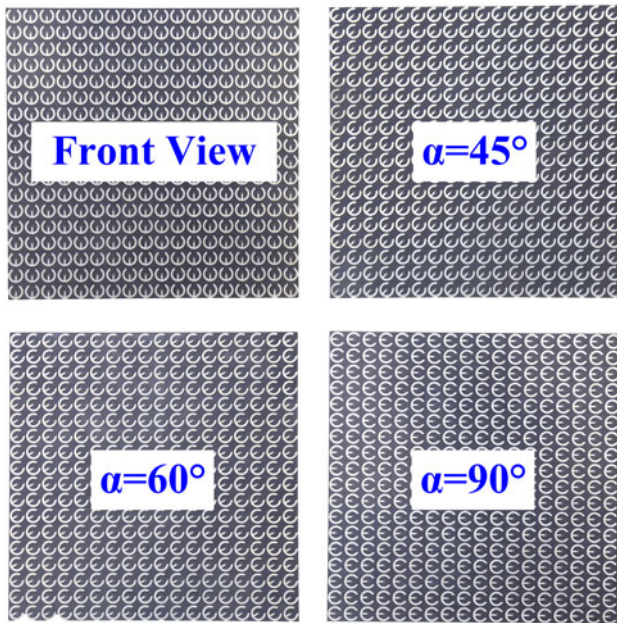


Fig. 6. The front and back views for the fabricated prototypes $\alpha = 45, 60, 90^\circ$.

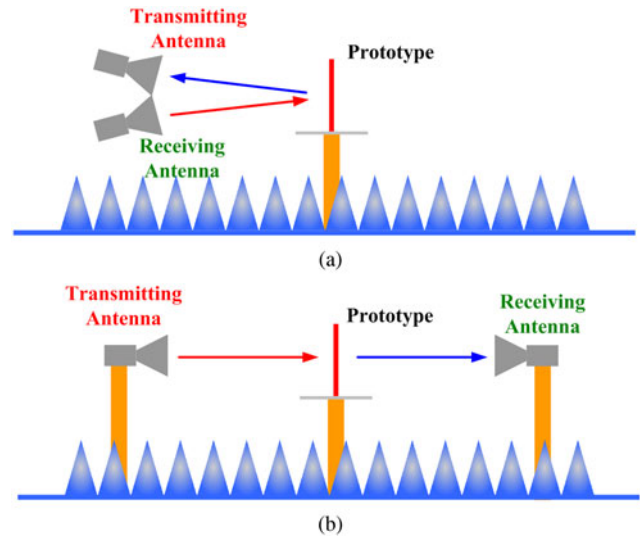


Fig. 7. The experimental setups for (a) reflection coefficient and (b) transmission coefficient.

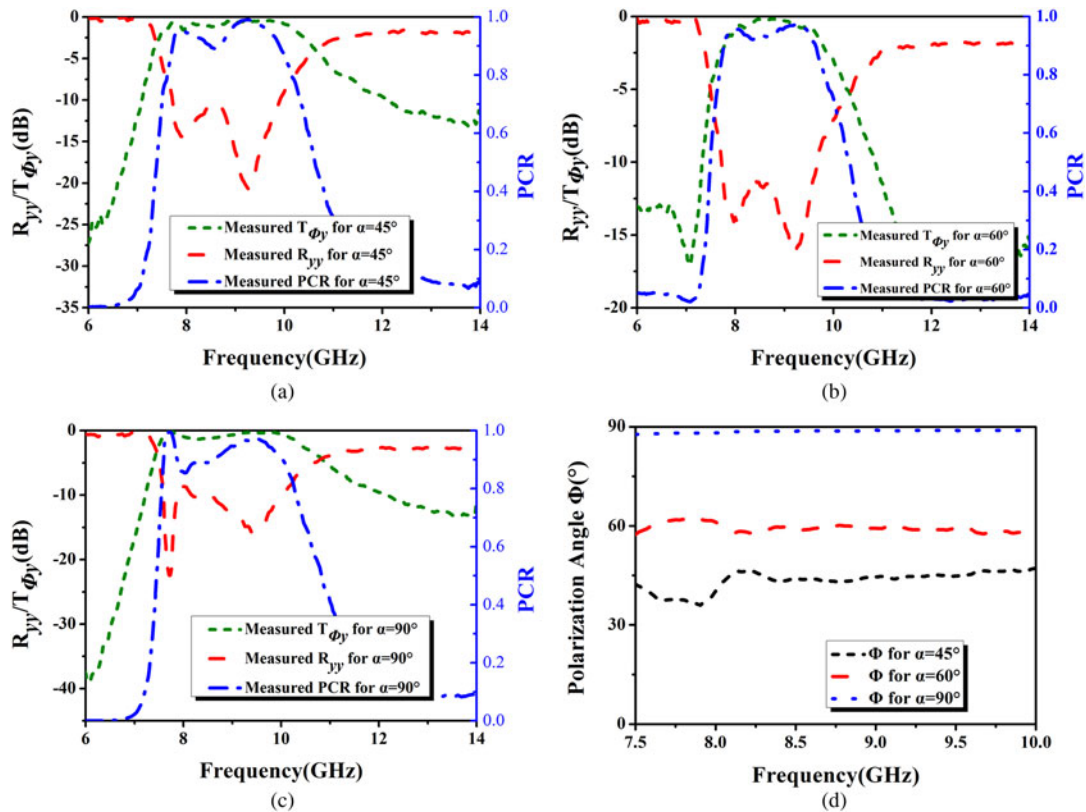


Fig. 8. (a, b, and c) The measured R_{yy} , $T_{\phi y}$ in dB and the corresponding PCR and (d) the deflected polarization angles Φ for $\alpha = 45, 60, 90^\circ$.

More intuitively, the E -field distributions at 9.6 GHz are given in Fig. 4, where it can obviously observe a deflection with respect to the polarization angle of normal incidence. For

further verification, the $T_{\phi y}$ in dB and the corresponding polarization conversion angles from $\alpha = 10$ to 90° with a 10° step are also simulated using the same simulated method. As shown in

Fig. 5(a), all the T_{Φ_y} remain to be more than -0.5 dB within an identical frequency band. The deflected polarization angles are still generally equal to the corresponding rotation angles, as the colorful curves plotted in Fig. 5(b). This characteristic can provide more conveniences for meeting diverse needs in practical applications.

Experimental results and analysis

For experimental validation, three samples with $\alpha = 45, 60, 90^\circ$ were fabricated by printed circuit board technology, as shown in Fig. 6. All the size is identically an area of $180 \text{ mm} \times 180 \text{ mm}$. The reflection (R_{xy} and R_{yy}) and transmission (T_{xy} and T_{yy}) coefficients were measured by a pair of horn antenna and a network analyzer (Agilent N5230C). To be out of the near field, each prototype is at least 3 m away from two horn antennas. As indicated by the reflection coefficient experimental setup in Fig. 7(a), two horn antennas are closely placed on the left side of the prototype. The in-between separation angle is lower than 6° . The transmission coefficient experimental setup is given in Fig. 7(b). It can be seen that two horn antennas are symmetrically placed on either side of the prototype. The centers of two antennas and the prototype locate at the same height. For eliminating errors from the measured environment, the results are normalized with ones without inserting prototypes. In order to achieve good polarization matching, the E -field of transmitting horn antenna in both setups is parallel to the axis of symmetry of the top SRRs. The receiving and transmitting horn antennas keep the same polarization state in the co-reflection/transmission coefficient measurement, whereas they are in the orthogonal state when measuring the cross-reflection/transmission coefficient.

Under normal y -polarized incidence, the measured T_{Φ_y} corresponding to $\alpha = 45, 60, 90^\circ$ are more than $-0.9, -1.3,$ and -0.7 dB in a frequency interval of 7.5–10 GHz, while the averaged PCRs are about 92.2, 88.9, and 91.9%, as shown in Fig. 8(a)–8(c). The deflected polarization angles Φ by post processing are averagely $43.2, 59.6,$ and 88.6° , basically equal to the corresponding rotation angles ($45, 60,$ and 90°), as plotted in Fig. 8(d). The averaged PCRs in simulation are approximately 96.7, 95.1, 97.1%, while the deflected polarization angles Φ on average are $44.3, 59.3,$ and 89.1° . The compared differences are mainly brought in the final stack and wed. Additionally, the F4B used in fabrication is not exactly the same as that in simulation, which also causes a negative impact on the performance of the polarization conversion efficiency.

Conclusion

In conclusion, an antenna-to-antenna method for a high-efficiency polarization converter for customized polarization angle deflection numerically and experimentally validated in this paper. Owing to the linear polarization state in operating, two in-linked SRRs are respectively utilized as the energy receiver and transmitter. Resulting from strong coupling between electric resonance and magnetic resonance, the converter has been proven to possess broadband and high polarization conversion efficiency. Particularly, the deflected polarization angle of the transmitted waves is generally consistent with the rotation angle of the bottom transmitting SRRs. This means the proposed method can achieve 90° polarization angle deflection as most published studies do, but also a customized one. Furthermore, a reconfigurable polarization converter can also be obtained by adding mechanization design and electronic controller in practical applications.

References

- Ludwig AC (1973) The definition of cross polarization. *IEEE Transactions on Antennas and Propagation* **21**, 116–119.
- Sun SL, He Q, Xiao SY, Xu Q, Li X and Zhou L (2012) Gradient-index metasurface as bridge linking propagating waves and surface waves. *Nature Materials* **11**, 426–431.
- Dong DX, Xia S, Zhuang YY, Shi HY, Zhang Z, He YC, Zhang AX, Wei XY and Xu Z (2017) Wideband polarization-independent anomalous reflection metasurface with multiple resonance modes. *Journal of Advanced Dielectrics* **07**, 1750010.
- Yu NF, Genevet P, Kats MA, Aieta F, Tetienne JP, Capasso F and Gaburro Z (2011) Light propagation with phase discontinuities: generalized laws of reflection and refraction. *Science* **334**, 333.
- Born M, Wolf E and Hecht E (2000) *Principles of Optics: Electromagnetic Theory of Propagation, Interference and Diffraction of Light* Physics Today **53**, 77–78.
- Zhang S, Park YS, Li JS, Lu XC, Zhang WL and Zhang X (2009) Negative refractive index in chiral metamaterial. *Physical Review Letters* **102**, 023901.
- Li ZF, Mutlu M and Ozbay E (2013) Chiral metamaterials: from optical activity and negative refractive index to asymmetric transmission. *Journal of Optics* **15**, 023001.
- Grady NK, Heyes JE, Chowdhury DR, Zeng Y, Reiten MT, Azad AK, Taylor AJ, Dalvit DAR and Chen HT (2013) Terahertz metamaterials for linear polarization conversion and anomalous refraction. *Science* **340**, 1304.
- Wang N, Liu Q, Wu C, Talbi L, Zeng Q and Xu J (2014) Wideband Fabry–Perot resonator antenna with two complementary FSS layer. *IEEE Transactions on Antennas and Propagation* **62**, 2463–2471.
- Muhammad SA, Sauleau R, Valerio G, Coq LL and Legay H (2013) Self-polarizing Fabry–Perot antennas based on polarization twisting element. *IEEE Transactions on Antennas and Propagation* **61**, 1032–1040.
- Li ZF, Mutlu M and Ozbay E (2014) Highly asymmetric transmission of linearly polarized waves realized with a multilayered structure including chiral metamaterials. *Journal of Physics D: Applied Physics* **47**, 075107.
- Fu XM, Wang JF, Fan Y, Feng MD, Yan MB, Li YF, Chen HY, Zhang JQ and Qu SB (2018) Merging bands of polarization converters by suppressing Fano resonance. *Applied Physics Letters* **113**, 101901.
- Shi JH, Ma HF, Guan CY, Wang ZP and Cui TJ (2014) Broadband chirality and asymmetric transmission in ultrathin 90° -twisted Babinet-inverted metasurface. *Physical Review B* **89**, 165128.
- Gao X, Han X, Cao WP, Li HO, Ma HF and Cui TJ (2015) Ultrawideband and high-efficiency linear polarization converter based on double V-shaped metasurface. *IEEE Transactions on Antennas and Propagation* **63**, 3522–3530.
- Chen HY, Wang JF, Ma H, Qu SB, Xu Z, Zhang AX, Yan MB and Li YF (2014) Ultra-wideband polarization conversion metasurface based on multiple plasmon resonances. *Journal of Applied Physics* **115**, 154504.
- Pfeiffer C and Grbic A (2013) Cascaded metasurface for complete phase and polarization control. *Applied Physics Letters* **102**, 231116.
- Li ZF, Gokkavas M and Ozbay E (2013) Chiral structures: manipulation of asymmetric transmission in planar chiral nanostructures by anisotropic loss. *Advanced Optical Materials* **1**, 482–488.
- Su P, Zhao YJ, Jia SL, Shi WW and Wang HL (2016) An ultra-wideband and polarization-independent metasurface for RCS reduction. *Scientific Reports* **6**, 20387.
- Li K, Liu Y, Jia YT and Guo YJ (2017) A circularly polarized high gain antenna with low RCS over a wideband using chessboard polarization conversion metasurface. *IEEE Transactions on Antennas and Propagation* **65**, 4288–4292.
- Jia YT, Liu Y, Guo YJ, Li K and Gong SX (2017) A dual patch polarization rotation reflective surface and its application to ultra-wideband RCS reduction. *IEEE Transactions on Antennas and Propagation* **65**, 3291–3295.
- Altintas O, Unal E, Akgol O, Karaaslan M, Karadag F and Sabah C (2017) Design of a wide band metasurface as a linear to circular polarization converter. *Modern Physics Letters* **31**, 509–594.

22. **Derin O, Karaaslan M, Unal E, Karadag F, Altintas O and Akgol O** (2019) Exhibition of polarization conversions with asymmetric transmission theory, natural like chiral, artificial chiral nihility and retrieval studies for K- and C-band radar applications. *Bulletin of Materials Science* **42**, 191.
23. **Chen Q and Zhang H** (2018) Dual-patch polarization conversion metasurface-based wideband circular polarization slot antenna. *IEEE Access* **6**, 74772–74777.
24. **Chen Q and Zhang H** (2019) High-gain circularly polarized Fabry–Perot patch array antenna with wideband low-radar-cross-section property. *IEEE Access* **7**, 8885–8889.



smart antennas, and electromagnetic compatibility.

Manlan Deng received the B.S degree from physics and communication electronic institute, Jiangxi Normal University in 2003. She joined department of electronics and information engineering of Yichun University in 2004 as an assistant teacher. She has been a lecturer in college of physical science and technology of Yichun University since 2011. Her research interests include computational electromagnetic,